Acta Crystallographica Section D
Biological Crystallography
ISSN 0907-4449

Structures of aminophenol dioxygenase in complex with intermediate, product and inhibitor

De-Feng Li,[a]‡ Jia-Yue Zhang,[b,c]‡ Yan-Jie Hou,[a,c] Lei Liu,[b,c] Yonglin Hu,[a] Shuang-Jiang Liu,[b]* Da-Cheng Wang[a]* and Wei Liu[d]*

[a]National Laboratory of Biomacromolecules, Institute of Biophysics, Chinese Academy of Sciences, Beijing 100101, People's Republic of China, [b]State Key Laboratory of Microbial Resources, Institute of Microbiology, Chinese Academy of Sciences, Beijing 100101, People's Republic of China, [c]Graduate School of Chinese Academy of Sciences, Beijing 100049, People's Republic of China, and [d]Institute of Immunology, The Third Military Medical University, Chongqing 400038, People's Republic of China

‡ These authors contributed equally to this work.

Correspondence e-mail: liusj@sun.im.ac.cn, dcwang@ibp.ac.cn, wei.liu.2005@gmail.com

Received 19 June 2012
Accepted 8 October 2012

PDB References: APD, apo, 3vsg; active enzyme with iron, 3vsh; complex with 4NC, 3vsi; complex with 3-iminooxepin-2(3*H*)-one and 2-aminomuconic 6-semialdehyde, 3vsj

Dioxygen activation by nonhaem Fe(II) enzymes containing the 2-His-1-carboxylate facial triad has been extensively studied in recent years. Here, crystal structures of 2-aminophenol 1,6-dioxygenase, an enzyme that represents a minor group of extradiol dioxygenases and that catalyses the ring opening of 2-aminophenol, in complex with the lactone intermediate (4*Z*,6*Z*)-3-iminooxepin-2(3*H*)-one and the product 2-aminomuconic 6-semialdehyde and in complex with the suicide inhibitor 4-nitrocatechol are reported. The Fe–ligand binding schemes observed in these structures revealed some common geometrical characteristics that are shared by the published structures of extradiol dioxygenases, suggesting that enzymes that catalyse the oxidation of noncatecholic compounds are very likely to utilize a similar strategy for dioxygen activation and the fission of aromatic rings as the canonical mechanism. The Fe-ligation arrangement, however, is strikingly enantiomeric to that of all other 2-His-1-carboxylate enzymes apart from protocatechuate 4,5-dioxygenase. This structural variance leads to the generation of an uncommon $O^{-}—Fe^{2+}—O^{-}$ species prior to O_2 binding, which probably forms the structural basis on which APD distinguishes its specific substrate and inhibitor, which share an analogous molecular structure.

1. Introduction

Iron-containing enzymes are employed by nature as a major strategy to activate the molecular oxygen essential for various processes involved in metabolism, oxidative phosphorylation and biodegradation. Among these enzymes, considerable attention has recently been focused on mononuclear nonhaem Fe(II) oxygenases and oxidases owing to the increased availability of structural, spectroscopic and computational data (Koehntop *et al.*, 2005; Straganz & Nidetzky, 2006; Bruijnincx *et al.*, 2008; Kovaleva & Lipscomb, 2008*b*). A common structural motif present in the active site of a specific nonhaem enzyme superfamily consists of two histidine side chains and one aspartate or glutamate side chain arranged at the vertices of one face of the iron-coordinating octahedron. Coined the 2-His-1-carboxylate facial triad, this structural feature found in extradiol dioxygenases, Rieske dioxygenases, α-ketoglutarate (α-KG) dependent enzymes, pterin-dependent enzymes and other oxidases serves as a versatile platform for dioxygen activation, effecting a wide range of oxidative transformations (Koehntop *et al.*, 2005; Bruijnincx *et al.*, 2008; Kovaleva & Lipscomb, 2008*b*).

Extradiol dioxygenase is the archetypal member of this large superfamily, which catalyses the oxygenolytic ring opening of aromatic compounds involved in microbial catabolism (Vaillancourt *et al.*, 2006; Kovaleva & Lipscomb, 2008*b*). The substrates are catechol analogues in most cases, but also include noncatecholic compounds such as gentisate, hydroquinone, salicylate and 2-aminophenol (Vaillancourt *et al.*, 2006). Abundant experimental and computational data have demonstrated that the catecholic substrate binds Fe(II) as a monoanion that arises from deprotonation of one of the vicinal hydroxyl substituents at the position closer to the C—C bond cleavage in the process of enzyme turnover (Horsman *et al.*, 2005; Vaillancourt *et al.*, 2002; Sato *et al.*, 2002). The resultant asymmetric binding leads to a change in the ligation state and electronic properties of the iron and consequently increases its affinity for O_2 (Fig. 1*c*; Shu *et al.*, 1995; Sato *et al.*, 2002). Upon dioxygen binding, electron density is transferred from the substrate to O_2 *via* Fe(II), yielding a nascent superoxide and an activated substrate (Fig. 1*d*; Kovaleva & Lipscomb, 2008*b*; Vaillancourt *et al.*, 2006). In the subsequent steps, an Fe(II) semiquinone is produced as a result of electron transfer from the substrate (Fig. 1*e*), and a concerted Criegee rearrangement assists in the immediate heterolysis of the O—O bond and inserts one O atom into the aromatic ring to form a lactone intermediate (Fig. 1*f*) before the formation of the final product (Fig. 1*g*) (Vaillancourt *et al.*, 2006). Despite these achievements in mechanistic understanding, whether this canonical mechanism applies to all enzymes, in particular to those that catalyse the reaction of noncatecholic substrates that lack vicinal hydroxyl substituents, remains unclear, as no such enzymes have been crystallographically characterized to date.

2-Aminophenol 1,6-dioxygenase (APD) represents a minor subset of enzymes that display no sequence or structural similarity to the majority of extradiol dioxygenases such as 2,3-dihydroxybiphenyl 1,2-dioxygenase (DHBD), catechol 2,3-dioxygenase (C23O) and homoprotocatechuate 2,3-dioxygenase (HPCD) (Vaillancourt *et al.*, 2006; Wu *et al.*, 2006) but that share a remote evolutionary ancestor with protocatechuate 4,5-dioxygenase (4,5-PCD; Noda *et al.*, 1990; Sugimoto *et al.*, 1999). The enzyme catalyzes the opening of 2-aminophenol (2AP) analogues at the position *ortho* to the hydroxyl substituent and generates a product such as 2-aminomuconic 6-semialdehyde (Fig. 1), thereby playing a vital role in the reductive pathway of microbial biodegradation of nitrobenzene (NB) and chlolorinated nitrobenzene (CNB) (Wu *et al.*, 2005, 2006). It shows amazing substrate selectivity towards 2AP, but is strongly inhibited by catechol analogues (Fig. 1). As the substrate 2AP differs from catechol in only one substituent (amino to hydroxyl), APD is thus an intriguing research target for study of the substrate specificity of enzymes that oxidize noncatechol compounds.

Since our knowledge of extradiol dioxygenases is mostly drawn from structural studies, we report here the crystal structures of APD from *Comamonas* sp. strain CNB-1 as the apoenzyme, the holoenzyme and as complexes with the lactone intermediate (4*Z*,6*Z*)-3-iminooxepin-2(3*H*)-one and the product 2-aminomuconic 6-semialdehyde and with the suicide inhibitor 4-nitrocatechol. The subunit structure of APD shows a similar fold to the catalytic subunit of 4,5-PCD, while the three-dimensional arrangement of ligand binding to the iron is distinctively enantiomeric to those in all previously reported structures of 2-His-1-carboxylate facial triad-containing enzymes apart from 4,5-PCD. These structural features expand our understanding from the canonical extradiol dioxygenases to those that catalyze noncatechol compounds and account well for the high substrate specificity of the enzyme.

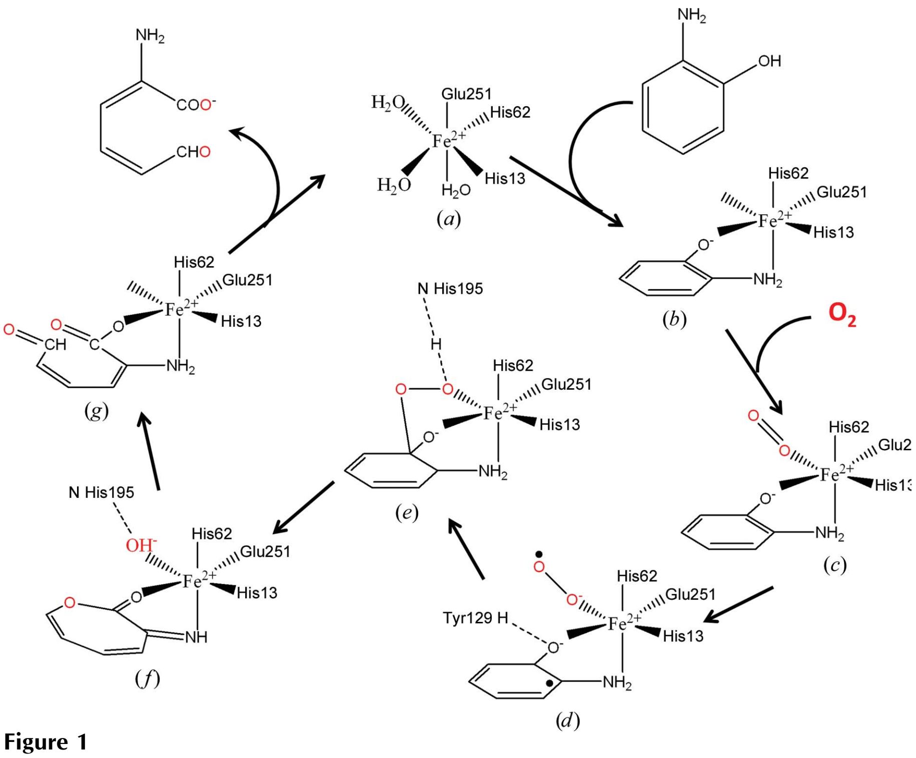

Figure 1
Proposed reaction mechanism for catalysis of the ring-cleavage of 2-aminophenol by APD. The O atoms from O_2 are highlighted in red.

2. Materials and methods

2.1. Purification and crystallization

Wild-type 2-aminophenol-1,6-dioxygenase from *Comamonas* sp. strain CNB-1 ($APD_{CNB\text{-}1}$) was purified from laboratory-cultured bacterial cells as described previously (Wu *et al.*, 2005). Selenomethionine-substituted protein was produced from the same strain grown in M9 minimal medium supplemented with L-selenomethionine. The methionine-pathway inhibition protocol was used to obtain maximal incorporation (Doublié, 1997).

Table 1
Summary of MAD data collection and phasing for Fe-free APD.

Values in parentheses are for the highest resolution shell.

	Peak	Inflection	Remote
Data collection			
Wavelength (Å)	0.9792	0.9794	0.9642
Space group	$C2$	$C2$	$C2$
Unit-cell parameters			
a (Å)	270.67	269.85	272.05
b (Å)	48.76	48.51	48.73
c (Å)	108.82	108.59	109.68
α (°)	90	90	90
β (°)	109.86	110.10	109.68
γ (°)	90	90	90
Resolution (Å)	69.17–2.60 (2.74–2.60)	68.68–2.70 (2.85–2.70)	69.50–2.70 (2.85–2.70)
Completeness (%)	99.2 (93.0)	99.9 (99.1)	99.8 (98.7)
Unique reflections	41350 (5544)	36876 (5264)	37677 (5355)
Multiplicity	7.0 (5.4)	3.6 (3.4)	3.6 (3.3)
$R_{\rm merge}$ (%)	8.8 (42.4)	9.3 (45.4)	9.7 (47.2)
Average $I/\sigma(I)$	18.7 (3.0)	12.1 (2.2)	11.8 (2.0)
Phasing			
Se-atom sites	29		
Overall figure of merit	0.63		

Table 2
Summary of X-ray data collection and refinement.

Values in parentheses are for the highest resolution shell.

	Fe-free APD	Active APD	APD–2AP	APD–4NC
Data collection				
Wavelength (Å)	1.5418	1.0000	1.5418	1.0000
Space group	$C2$	$C2$	$C2$	$C2$
Unit-cell parameters				
a (Å)	269.73	265.39	270.24	272.73
b (Å)	48.26	47.47	48.39	48.26
c (Å)	108.44	107.38	108.55	108.12
β (°)	109.44	109.47	109.57	109.61
Resolution (Å)	39.78–2.40 (2.53–2.40)	47.95–2.70 (2.85–2.70)	39.87–2.30 (2.42–2.30)	69.3–2.50 (2.64–2.50)
Completeness (%)	91.8 (82.5)	98.1 (93.7)	97.8 (86.5)	91.0 (81.6)
No. of unique reflections	48049 (6247)	34673 (4756)	58265 (7456)	42370 (5494)
Multiplicity	4.5 (4.4)	3.2 (2.6)	5.2 (3.9)	3.2 (2.9)
$R_{\rm merge}$ (%)	7.3 (32.3)	10.3 (33.3)	10.9 (35.6)	4.7 (33.6)
Average $I/\sigma(I)$	20.6 (4.4)	11.5 (2.7)	15.7 (2.7)	18.2 (3.2)
Structure refinement				
$R_{\rm work}$ (%)	18.5	17.5	19.0	20.5
$R_{\rm free}$ (%)	24.6	24.7	23.3	27.0
R.m.s.d. bond angles (°)	1.47	1.12	1.03	1.09
R.m.s.d. bond lengths (Å)	0.007	0.007	0.006	0.007
Ramachandran plot				
Core region (%)	86.6	89.8	89.8	88.2
Allowed region (%)	12.7	9.6	9.3	11.4
Generously allowed region (%)	0.4	0.6	0.7	0.2
Disallowed region (%)	0.3	0	0.2	0.1

The purified apoenzyme was concentrated to approximately 10 mg ml^{-1} in a solution consisting of 50 mM Tris pH 8.0, 5% glycerol, 2 mM DTT, 0.2 mM EDTA prior to crystallization trials. Crystals of metal-free APD were grown in 25% PEG 3350, 0.2 mM sodium chloride, 0.1 M sodium cacodylate pH 6.5 by the hanging-drop method at room temperature under ambient aerobic conditions. Crystallization drops for the active enzyme were set up under the same conditions in the presence of 5 mM $FeSO_4$. Complex crystals were prepared by cocrystallization of the holoenzyme with the addition of 5 mM 2-aminophenol (2AP) or 4-nitrocatechol (4NC).

2.2. Data collection

The crystals used for data collection were dipped into cryoprotectant (reservoir solution supplemented with 10% glycerol) for roughly 10 s before being mounted in nylon CryoLoops (Hampton Research) and flash-cooled in a stream of liquid nitrogen at 95 K. X-ray data collections for active APD and the complex with 4NC were carried out on beamline NW12A at KEK, Photon Factory, Japan using a wavelength of 1.0 Å. Multiwavelength anomalous diffraction (MAD) data for the selenomethionyl derivative were also collected on beamline NW12A using three wavelengths: 0.9792, 0.9794 and 0.9642 Å. Native data sets for the apoenzyme and the complex with 2AP were collected using an in-house Rigaku R-AXIS IV^{++} image plate and a Cu $K\alpha$ radiation source (λ = 1.5418 Å). All diffraction data were evaluated using *MOSFLM* and *SCALA* from the *CCP*4 program suite (Winn *et al.*, 2011; Rossmann & van Beek, 1999). Further details of APD purification, crystallization and data collection are given in Li *et al.* (2012).

2.3. Structure determination and refinement

The structure of metal-free inactive APD was determined using the MAD technique. Phase calculation and density modification were performed using the *SOLVE*/*RESOLVE* program suite (Terwilliger, 2004). A partial model was automatically established and the rest of the model was manually built using the graphics package *O* (Jones *et al.*, 1991). The structure was refined using *CNS* (Brünger *et al.*, 1998). The refined model was subsequently used as a search template in structure determinations of the active enzyme and the APD–2AP and APD–4NC complexes using molecular replacement. Refinement of these structures was performed using *CNS* and *REFMAC*5 (Murshudov *et al.*, 2011) with manual modelling between refinement cycles. The final models were validated using the *CCP*4 program *PROCHECK* (Laskowski *et al.*, 1993) to control stereochemical quality. Two α subunits and two β subunits forming a moderately compact tetramer are present in the asymmetric unit of all crystals. The statistics of data collection, MAD phasing and structure refinement are given in Tables 1 and 2. All figures representing APD structures were prepared using the *PyMOL* molecular-graphics program (http://www.pymol.org).

2.4. Ligand modelling and refinement

In the enzyme–substrate complex structure, the lactone intermediate 3-iminooxepin-2(3*H*)-one and the product 2-aminomuconic 6-semialdehyde were modelled into the β subunits *D* and *B*, respectively. To obtain the best fit to the diffraction data, $F_{\rm obs} - F_{\rm calc}$ electron density contoured at 3.5σ was used for this modelling work. Likewise, the suicide inhibitor 4NC was modelled into both catalytic subunits of the enzyme–inhibitor complex structure. The ligand dictionaries for 3-iminooxepin-2(3*H*)-one and 2-aminomuconic 6-semialdehyde were generated from imported PDB files using the *CCP*4 program *Monomer Sketcher* after running *REFMAC*5 to idealize the ligand structures and that for 4NC was downloaded from the HIC-Up database (Kleywegt, 2007). The atom indices of all ligands were renumbered to maintain consistency with those shown in Fig. 1. Model bias introduced by ligand modelling was minimized by real-space refinement in the annealed OMIT maps generated in the absence of active-site ligands. The distances between the amino or hydroxyl groups of the ligands and Fe were not restrained during refinement. In the last round of refinement, a ligand-free model was generated by setting the occupancies of all atoms of the ligands to zero and allowing them to be refined for ten cycles. The resultant positive density (>3.5σ) in an OMIT difference map ($F_{\rm obs} - F_{\rm calc}$) was checked to determine whether it overlays well with ligand $2F_{\rm obs} - F_{\rm calc}$ density after ten cycles of full model refinement.

2.5. Enzyme-kinetics measurements

Catalytic kinetics measurements of APD on 2AP and catechol were performed at room temperature by monitoring the increase in absorbance at 380 nm for 2AP (Wu *et al.*, 2005) and at 375 nm for catechol. The reaction solution buffered at pH 8.0 contained 0.16 m*M* 2AP or catechol. The $K_{\rm m}$ value was calculated from Lineweaver–Burke plots using the following molar extinction coefficients: 15 100 M^{-1} cm^{-1} for 2AP (Lendenmann & Spain, 1996) and 33 000 M^{-1} cm^{-1} for catechol (Iwagami *et al.*, 2000). The $K_{\rm m}$ of O_2 on different substrates was obtained polarographically from plots with an oxygen concentration ranging from 0 to 1200 µ*M*. Reaction buffers containing different oxygen concentrations were prepared by vigorously bubbling with a humidified mixture of O_2 and N_2 gas for at least 60 min prior to the experiment, and

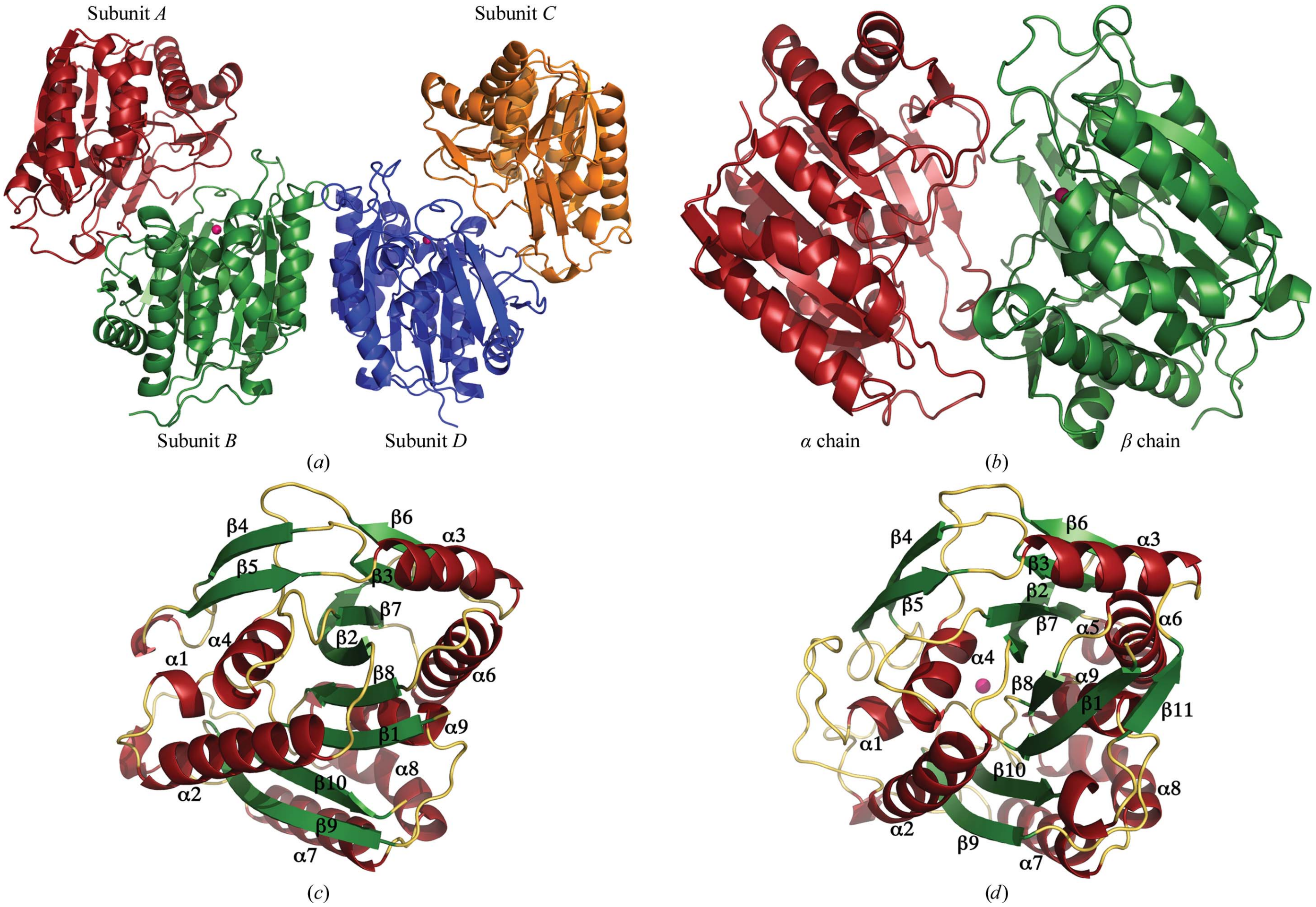

Figure 2
The overall structure and subunit fold of APD. (*a*) Ribbon model of an APD tetramer with an $\alpha_2\beta_2$ assembly. (*b*) Ribbon model of an $\alpha\beta$ dimer. (*c*) Fold of the α subunit. (*d*) Fold of the β subunit. The iron centre is represented by a magenta sphere.

the dioxygen partial pressure was controlled by adjusting the O_2:N_2 ratio in the gas mixture.

For the inhibition experiment, the purified enzyme was incubated with 0.2 m*M* catechol before measuring the remaining catalytic activity towards 2AP. Subsequently, the reaction solution was applied onto a desalting column (HiTrap 5 ml, GE Healthcare) to remove catechol and the enzyme was incubated with 2 m*M* $FeSO_4$ and 5 m*M* ascorbate for 2 h at 277 K before measuring the recovered enzymatic activity.

2.6. Site-directed mutagenesis

The ORF encoding full-length APD was inserted into the expression plasmid pET28a, which was subsequently transformed into *Escherichia coli* strain BL21 (DE3) to produce the recombinant enzyme. A series of constructs for mutations in the β subunit were made by the PCR method. The mutations included H13A, H62A, E251A, Y129F and H195Q. The mutant proteins were purified using the same protocol as used for the native enzyme.

3. Results

3.1. Overall structure and subunit fold

We crystallized the APD protein from *Comamonas* sp. strain CNB-1 with and without ferrous ion and in complexes with 2AP and with the suicide inhibitor 4-nitrocatechol (4NC). The structures were refined at resolutions from 2.3 to 2.7 Å (Table 2). The overall structure of APD shows an $\alpha_2\beta_2$ assembly with a crescent shape (Fig. 2*a*). The tetramer is composed of two tightly bound $\alpha\beta$ heterodimers, each of which forms an independent catalytic unit (Fig. 2*b*). The two β subunits contact each other in a back-to-back manner, but there is a lack of direct contacts between the α subunits. The α and β subunits of APD are related in sequence (Fig. 3*a*) and,

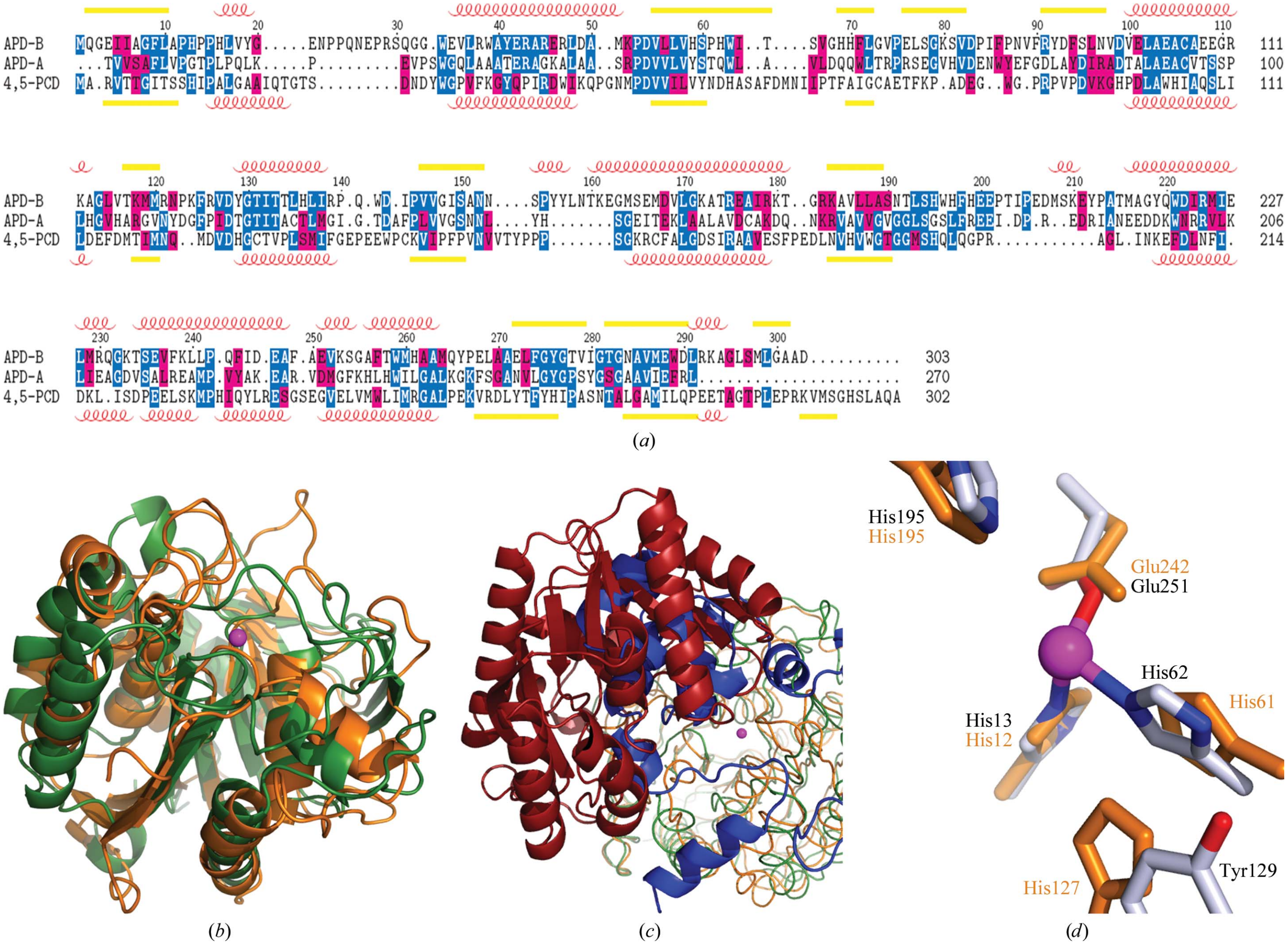

(*a*)

(*b*) (*c*) (*d*)

Figure 3
Sequence and structural comparison between APD and 4,5-PCD. (*a*) Structure-based sequence alignment of the β and α chains of APD (APD-B and APD-A, respectively) and the β chain of 4,5-PCD. The secondary-structure elements of APD and 4,5-PCD are labelled on the top and bottom lines, respectively. (*b*) Structure superimposition on the β subunit of both enzymes: APD is in green and 4,5-PCD is in gold. The Fe atom is represented by a magenta sphere. (*c*) Superimposition of the $\alpha\beta$ dimeric structures, with the α subunit of APD in red and that of 4,5-PCD in light blue. (*d*) Overlay of active sites. The model of APD is colour coded by atom (C in grey, N in blue, O in red and Fe in magenta) and that of 4,5-PCD in gold. The labels for APD and 4,5-PCD are in black and gold, respectively.

as expected, display almost identical folds (Figs. 2*c* and 2*d*). Both subunits comprise ten β-strands, nine α-helices and two 3_{10}-helices, with the major β-sheet sandwiched between two helical clusters.

3.2. Comparison with protocatechuate 4,5-dioxygenase

In the extradiol dioxygenase superfamily, APD and 4,5-PCD are thought to be evolutionarily related, although 4,5-PCD catalyzes the cleavage of vicinal hydroxyl compounds while APD is active towards noncatechol substrates (Vaillancourt *et al.*, 2006). Both enzymes have $\alpha_2\beta_2$-type subunit compositions. Despite the low sequence identity of below 15% between their catalytic subunits (Fig. 3*a*), the two enzymes basically share the same fold, with an r.m.s.d. of 1.7 Å on structure superimposition with 229 aligned C^α atoms (Fig. 3*b*). The active sites of both enzymes are located in a cleft in the β subunit close to a surface extensively covered by the α subunit. The iron in APD is coordinated in a distorted pyramidal geometry by residues His13, His62 and Glu251, which correspond to His12, His61 and Glu242, respectively, in 4,5-PCD.

Despite these similarities, some significant differences between APD and 4,5-PCD were observed. Firstly, APD appears to have evolved through a gene-duplication event as its two subunits are homologous in sequence, but the two subunits of 4,5-PCD are unrelated. Secondly, the quaternary structure differs between them, although both exist as stable $\alpha_2\beta_2$ tetramers. APD displays a crescent arrangement, while 4,5-PCD shows a more compact assembly (Sugimoto *et al.*, 1999). Even so, there is a lack of direct contacts between the two α subunits in both structures. Thirdly, the accessibility of substrates toward the active sites varies between the enzymes because of the different fold and orientation of the α subunit in the structures. In 4,5-PCD the iron centre is completely covered by a lid composed of two helices from the α subunit, while its counterpart in APD is only partially covered by the α subunit (Fig. 3*c*). Consequently, the active site of APD is more open than that of 4,5-PCD.

3.3. The iron centre

Perfect electron density for the iron was observed in the density map of the Fe-containing structure but not in the Fe-free structure. The ferrous centre is present in the β subunit only, as the α subunit lacks the 2-His-1-carboxylate facial triad for iron coordination in its sequence. The Fe(II) ion is located midway in a groove between the central β-sheet and a helical cluster composed of $\alpha1$, $\alpha2$ and $\alpha4$ in the catalytic subunit (Fig. 3*b*) and is coordinated by His13, His62 and Glu251. Another two residues, Tyr129 and His195, are involved in forming the second shell of the iron-coordination sphere. The geometric arrangement of the Fe ligands is identical in APD and 4,5-PCD (Fig. 3*d*). The only notable difference is that in the second shell of the iron-coordination sphere Tyr129 in APD is replaced by a histidine residue (His127) in 4,5-PCD. The substitution at this position may at least partially account for the different substrate preferences of the two enzymes.

3.4. Ligand modelling in the APD–2AP complex structure

Although the enzyme–substrate crystal was grown with the addition of 2AP, we thought it unreasonable to model the substrate itself in the complex structure because (i) the crystal was grown under aerobic conditions and 2AP has been reported to be very susceptible to oxygen and (ii) inactivation of APD by an excess of 2AP has never been observed in enzymatic assays by ourselves or other laboratories; this is a feature that is distinct from most extradiol dioxygenases, which can be inhibited by their own substrates, *e.g.* HPCD and 4,5-PCD. In fact, we have observed that the enzyme remains active in catalyzing the fission of 2AP even *in crystallo*, albeit with a much slower rate than in solution.

After cycles of refinement of the protein model of the complex structure, ligand density in the $F_{\rm obs} - F_{\rm calc}$ map became very clear at contours above 3.5σ. In one of the catalytic subunits (*D*), intact circular density was clearly observed opposite His62 and Glu251, and spherical density perfect for a superoxide ion or solvent molecule was present opposite to His13. The circular density showed imperfect planarity and the encircled contour seemed to be more appropriate to accommodate a seven-membered ring than a six-membered ring. It appears that O—O bond cleavage had already occurred since no density to accommodate a dioxygen molecule was observed around Fe(II). Considering all of these experimental observations, a lactone intermediate, 3-imino-oxepin-2(3*H*)-one (Fig. 1*f*), was modelled into the density opposite His62 and Glu251. Consistent with this, a superoxide ion was placed into the density opposite His13 since one O atom from the dioxygen was already incorporated into the substrate ring (Fig. 4*a*).

However, the ligand density in the other catalytic subunit (*B*) appeared to be different. The circular electron density shown in the $F_{\rm obs} - F_{\rm calc}$ map opposite His62 and Glu251 appeared broken in comparison with that in subunit *D*. This density also remained discontinuous in the $2F_{\rm obs} - F_{\rm calc}$ map even after ten cycles of restrained refinement after modelling different intermediates in this subunit, which indicates that a ligand with an opened ring is more likely to be present here. Therefore, the product of the 2AP fission reaction, 2-aminomuconic 6-semialdehyde, was modelled in this site (Fig. 4*c*). The fit of this ligand to the density did not seem to be as good as the fit in subunit *D*, probably because of the higher ligand flexibility resulting from ring opening. The occupancy of this ligand was accordingly adjusted to 0.7 to maintain reasonable *B* factors parallel to those of the ligand in subunit *D*. A solvent molecule was added *trans* to His13 since both O atoms from the dioxygen have been incorporated into the product.

Ligand modelling in both catalytic subunits led to a significant decrease in $R_{\rm free}$, good fitting to the electron density and reasonable Fe–ligand distances and other stereochemical parameters, all of which indicate correct modelling.

3.5. Symmetric intermediate/product binding

Presumably, the correct modelling means that the substrate has been oxidized in the crystal such that the hydroxyl substituent of 2AP has become a carbonyl group in the intermediate 3-iminooxepin-2(3*H*)-one and a carboxyl group in the product 2-aminomuconic 6-semialdehyde, while the amino substituent of 2AP has become an imine in both ligands. The iron is assumed to be in the ferrous state in both subunits since the enzyme apparently remains active towards its substrate. As shown in Figs. 4(*b*) and 4(*d*), both ligands bind the iron in such a way that O^{2AP} of the substrate takes up the position opposite to Glu251 and N^{2AP} occupies the site *trans* to His62, leaving an adjacent position *trans* to His13 for dioxygen binding. Almost equal $Fe^{2+}-O$ and $Fe^{2+}-N$ distances of 2.4–2.5 Å indicate symmetric binding of both ligands to the iron (Fig. 4 and Table 3), which is reasonable because of the non-ionic form of the ligands subsequent to O—O bond cleavage. In addition, the Fe–ligand distances are obviously longer than the averaged distances in the published crystal structures of extradiol dioxygenases containing deprotonated hydroxyls, yet are in good agreement with those in the case of carbonyl/carboxyl O and imine N.

The vicinal His195 effectively stabilizes the bound ligand in both cases by forming hydrogen bonds to the imine group. However, Tyr129, another key residue involved in the second Fe-coordination shell, does not directly contact the ligands, as is the case observed in other published structures (Shu *et al.*, 1995; Vaillancourt *et al.*, 2006; Kovaleva & Lipscomb, 2007), where Tyr129 invariably forms a tight hydrogen bond to the deprotonated hydroxyl of the substrate. In this case, the side chain of Tyr129 forms a hydrogen bond to His62 instead (Figs. 4*b* and 4*d*). The unusual behaviour of this residue provides another piece of evidence for an almost complete enzymatic reaction.

3.6. Asymmetric inhibitor binding

In the enzyme–inhibitor structure, the suicide inhibitor 4NC fits the electron density perfectly (Fig. 5*a*). It binds the iron with the same orientation as the intermediate, *i.e.* $O1^{4NC}$ (corresponding to N^{2AP}) occupies the Fe-coordination site

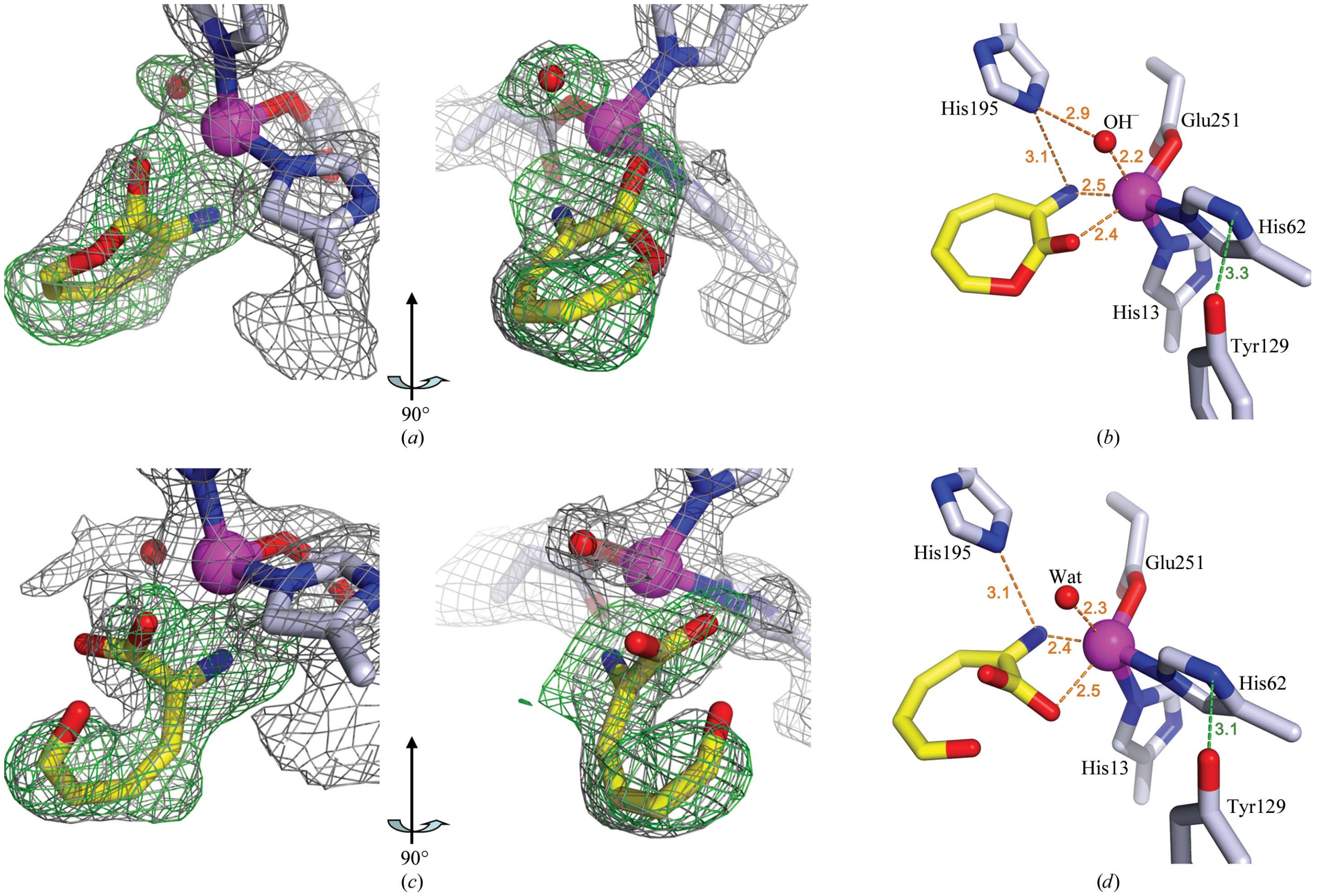

(*a*) (*b*)

(*c*) (*d*)

Figure 4
Fe ligandation in the structure of APD in complex with 3-iminooxepin-2(3*H*)-one and 2-aminomuconic 6-semialdehyde. (*a*) Lactone-intermediate complex (subunit *D*) fitting the electron density. (*b*) Stick model of the lactone intermediate and superoxide binding in the Fe(II) coordination sphere in subunit *D*. (*c*) Product complex (subunit *B*) fitting the electron density. (*d*) Stick model of product and a solvent molecule binding in the Fe(II) coordination sphere in subunit *B*. The grey $2F_{obs} - F_{calc}$ maps are contoured at 1.0σ and the green $F_{obs} - F_{calc}$ ligand-omit maps are contoured at 3.5σ. Element colour indices: carbon, grey (protein) or yellow (ligand); nitrogen, blue; oxygen, red; iron, magenta. Hydrogen bonds and 2AP–Fe^{2+} bonds are represented by dashed lines. Numbers indicate bond distances in Å.

Table 3
Bond distances (Å) in the Fe-coordination spheres.

Distance	Subunit *B* (*β*1)	Subunit *D* (*β*2)	Average
APD–3-iminooxepin-2(3*H*)-one			
Fe—N$^{\varepsilon}$ His13		2.1	
Fe—N$^{\varepsilon}$ His62		2.2	
Fe—O$^{\varepsilon}$ Glu251		2.0	
Fe—proximal O$^{\mathrm{ligand}\dagger}$		2.4	
Fe—N$^{\mathrm{ligand}}$		2.5	
APD–2-aminomuconic 6-semialdehyde			
Fe—N$^{\varepsilon}$ His13	2.2		
Fe—N$^{\varepsilon}$ His62	2.2		
Fe—O$^{\varepsilon}$ Glu251	2.0		
Fe—proximal O$^{\mathrm{ligand}}$†	2.5		
Fe—N$^{\mathrm{ligand}}$	2.4		
APD–4NC complex			
Fe—N$^{\varepsilon}$ His13	2.1	2.1	2.1
Fe—N$^{\varepsilon}$ His62	2.1	2.2	2.1
Fe—O$^{\varepsilon}$ Glu251	1.8	2.0	1.9
Fe—O2$^{\mathrm{4NC}}$‡	1.8	2.0	1.9
Fe—O1$^{\mathrm{4NC}}$§	2.4	2.3	2.3

† The proximal O$^{\mathrm{ligand}}$ corresponds to the hydroxyl O in the substrate, *i.e.* O$^{\mathrm{2AP}}$. ‡ O1$^{\mathrm{4NC}}$ occupies the same binding position in the Fe-coordination sphere as N$^{\mathrm{2AP}}$. § O2$^{\mathrm{4NC}}$ occupies the same binding position in the Fe-coordination sphere as O$^{\mathrm{2AP}}$.

trans to His62 and O2$^{\mathrm{4NC}}$ is positioned opposite Glu251. In this complex structure, 4NC binds Fe in an asymmetric manner, as the distances O1$^{\mathrm{4NC}}$—Fe and O2$^{\mathrm{4NC}}$—Fe are unequal (Fig. 5*b* and Table 3). The O2$^{\mathrm{4NC}}$—Fe bond length (1.9 Å) clearly indicates the deprotonated state and the monoanionic form of O2$^{\mathrm{4NC}}$. A tight hydrogen bond between O2$^{\mathrm{4NC}}$ and OH$^{\mathrm{Tyr129}}$ is formed to stabilize the monoanion of 4NC (Fig. 5*b*), which is in good agreement with published structures in which asymmetric binding occurs as a result of deprotonation of one hydroxyl group of the bound ligand (Kovaleva & Lipscomb, 2007, 2008*a*; Sato *et al.*, 2002). Consequently, a 45° rotation of the Tyr129 side chain between the structures is revealed on the superimposition of the two complex structures (Fig. 5*c*), indicating a high degree of flexibility and an important role of this amino acid in the process of enzyme turnover.

In contrast to the enzyme–substrate complex, the iron in the APD–4NC structure is presumed to be oxidized to Fe(III) because (i) the Fe–ligand distances are remarkably shorter than those in the other structures (Table 3) and conform to reported Fe^{3+}–ligand distances (Sugimoto *et al.*, 1999) and (ii) inactivated APD recovers its enzymatic activity to 100% upon incubation with Fe(II) and a reducing agent (see below).

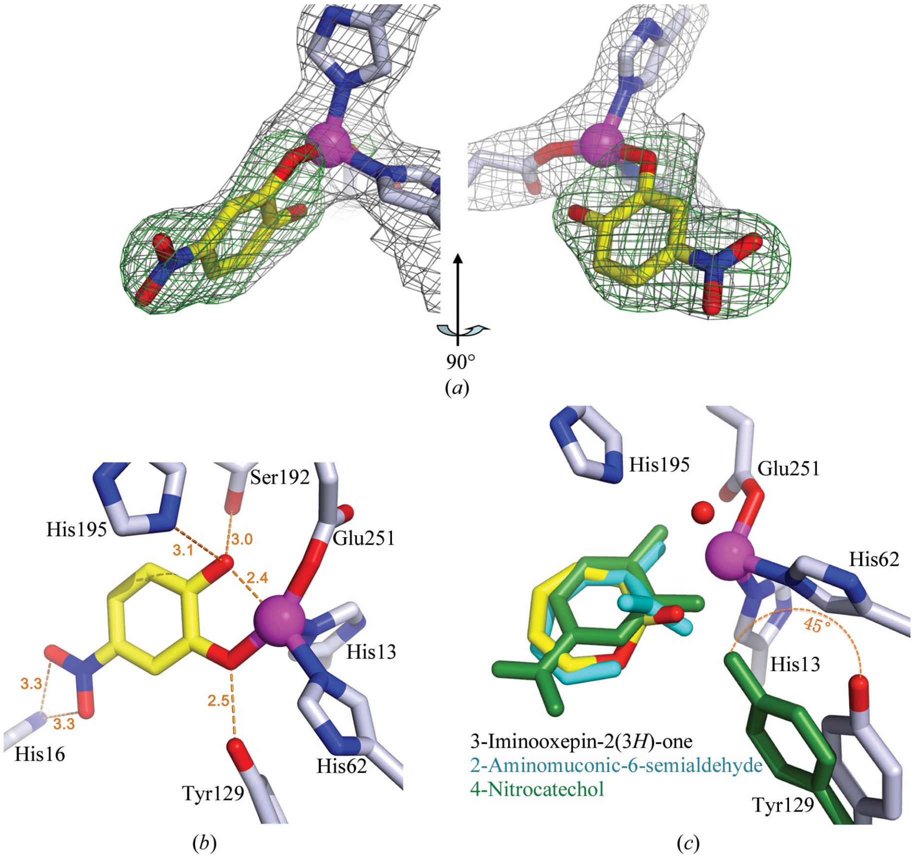

Figure 5
The complex trapped in the active sites of the APD–4NC structure. (*a*) 4NC fitting the electron density. (*b*) 4NC binding the iron oxidized from the ferrous state to the ferric state. Hydrogen bonds and the 4NC–Fe^{3+} interaction are represented by dashed lines. Numbers indicate bond distances in Å. (*c*) The Fe-coordination sphere with overlaid ligands: intermediate, product and 4NC. The APD intermediate model is denoted with atom-indexed colours; the product ligand is in cyan and the APD–4NC model is in green.

3.7. Enantiomeric Fe coordination

Although we did not straightforwardly observe substrate binding based on electron density, the binding mode of the substrate could indubitably be deduced from the complex structures determined in this study. Like the substrates of all other extradiol dioxygenases, 2AP would bind Fe in an asymmetric manner upon deprotonation and ionization of its hydroxyl substituent. The substrate binding in APD would be in such a way that $-\mathrm{O}^-$ occupies the position *trans* to Glu251 and the $-\mathrm{NH_2}$ group resides at the site *trans* to His62, leaving an adjacent site *trans* to His13 for dioxygen binding (Fig. 6*a*).

By comparison with published structures of 2-His-1-carboxylate enzymes, the three-dimensional arrangement of ligand binding to Fe in APD differs from that in all other enzymes except for 4,5-PCD (Fig. 6*b*). The configuration of Fe coordination shown in these two enzymes are effectively enantiomeric to those in other extradiol dioxygenases, *e.g.* HPCD (Fig. 6*c*), and *α*-KG-dependent enzymes, *e.g.* clavaminate synthase (Fig. 6*d*). One His and the Glu residue chelating Fe(II) exchange their locations in the APD and 4,5-PCD structures with respect to the other enzymes, forming a striking difference between these structures. Owing to this ligand-position exchange, the deprotonated hydroxyl of bound compounds is positioned uniquely *trans* to a Glu in APD and 4,5-PCD, rather than a His as in all other 2-His-1-carboxylate enzymes (Fig. 6, middle). As a result, the two monoanions coordinating Fe before O_2 binding, one from Glu and the other from the ligand, are aligned so as to form a linear $O^-—Fe^{2+}—O^-$ species in the minor group of extradiol dioxygenases represented by APD and 4,5-PCD (Fig. 6, bottom). In addition, the site for dioxygen binding is opposite a His in this group, which differs from HPCD but is identical to α-KG-dependent enzymes. All of these variations highlight the versatility of the 2-His-1-carboxylate platform that is shared among mononuclear nonhaem Fe(II) enzymes.

3.8. Kinetics assays

In kinetics measurements, K_m and V_{max} of 2AP and catechol for APD were calculated from Lineweaver–Burke plots (Fig. 7) to be 17.1 μM and 19.0 μM min^{-1} mg^{-1}, respectively; in comparison, those of catechol were 6.84 μM and 1.12 μM min^{-1} mg^{-1}, respectively. These data indicated that catechol has a threefold higher affinity for APD than 2AP, but that its catalytic efficiency was one order of magnitude lower than that of the latter. The results obtained in our experiment agreed well with previous reports for APDs from other sources (Takenaka *et al.*, 1997; Davis *et al.*, 1999). The K_m values for oxygen with the above compounds were also measured, but no remarkable variance was observed between them. K_{m,O_2} under 2AP and catechol incubation was 77.5 ± 5.1 and 58.3 ± 9.6 μM, respectively, which indicated that 2AP binding to the iron centre increases its affinity for O_2 with a comparable efficiency to monoanionic catechol binding.

3.9. Activity inhibition and recovery

It has been reported that the enzymatic activity of APD from *Pseudomonas pseudoalcaligenes* JS45 (APD_{JS45}) or *Pseudomonas* sp. AP-3 ($APD_{AP\text{-}3}$) catalyzing the ring opening of 2AP was inhibited in the presence of catechol analogues (Davis *et al.*, 1999; Takenaka *et al.*, 1997). In agreement with these published observations, we found that $APD_{CNB\text{-}1}$ completely lost its activity towards 2AP after incubation with catechol or 4NC for 100 s. The catalytic activity towards 2AP, however, was restored to 100% after removal of the catechol by applying the reaction mixture to a desalting column and subsequent incubation with 2 mM Fe^{2+} and 5 mM ascorbate on ice. These data provided biochemical evidence for the oxidation of Fe(II) to Fe(III) in enzyme inhibition.

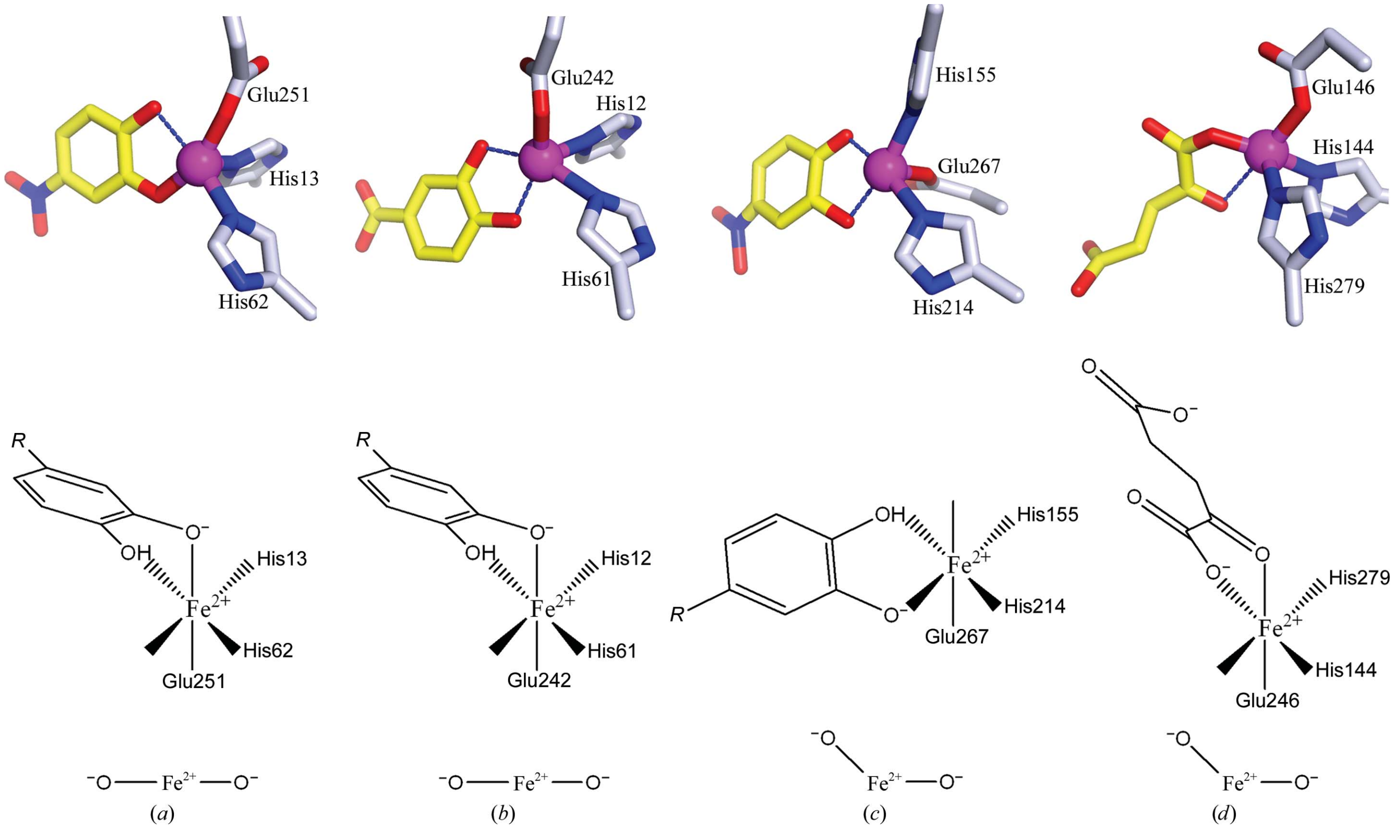

Figure 6

Comparison of Fe–ligand coordination geometry at the active site prior to O_2 binding in some 2-His-1-carboxylate enzymes. (*a*) The APD–4NC complex structure, (*b*) the 4,5-PCD structure (PDB entry 1b4u; Sugimoto *et al.*, 1999), (*c*) HPCD (PDB entry 2iga; Kovaleva & Lipscomb, 2007) and (*d*) the α-KG-dependent enzyme clavaminate synthase (CAS-α-KG-PCV; PDB entry 1drt; Zhang *et al.*, 2000). Schematic representations of the Fe-coordination scheme are shown in the middle and simplified representations showing Fe coordination with two O^- anions from the carboxylic side chain of the Glu residue and a hydroxyl substituent of the bound ligand are shown at the bottom.

3.10. Site-directed mutagenesis

Key amino acids involved in Fe coordination include His13, His62 and Glu251 in the first shell and Tyr129 and His195 in the second shell (Figs. 4 and 5). As expected, any single mutation of these residues led to a complete loss of enzymatic activity towards 2AP. Among the effective mutants, Y129F is particularly noteworthy as it highlights the important role of this residue as a hydrogen donor. The abolition of catalytic activity on its mutation implies a possible role of this residue in the deprotonation of the hydroxyl group of 2AP and the formation of a hydrogen bond between O^{2AP} and OH^{Tyr129} during enzyme turnover, although this was not observed *in crystallo*.

4. Discussion

The current mechanistic understanding of the aromatic ring fission catalyzed by extradiol dioxygenases was mostly achieved from investigations of the enzymes from the major class exemplified by DHBP (Sato *et al.*, 2002) and HPCD (Kovaleva & Lipscomb, 2007, 2008*a*); the other subsets, *e.g.* those represented by 4,5-PCD and APD, have been much less studied. The crystal structures of APD reported here provide a good opportunity to extend our knowledge of the 2-His-1-carboxylate facial triad from enzymes oxidizing canonical vicinal hydroxyl compounds to those catalyzing noncatechol substrates. The results obtained in our experiments also supply valuable hints for us to speculate how the minor group of extradiol dioxygenases distinguishes catechol and noncatechol compounds and whether it utilizes a similar catalytic mechanism to those in the major class.

In this study, two different ligands, the lactone intermediate and the product, bind the iron in the two catalytic subunits of one complex structure. Similar precedents have been found in other extradiol dioxygenases, *e.g.* HPCD (Kovaleva & Lipscomb, 2007, 2008*a*). All of these observations suggest that crystal-packing forces play an import role in stabilizing bound ligands at different stages of the catalytic cycle determined by the respective microenvironment. In this case, the intermediate fits the electron density in subunit *D* better than the product present in subunit *B* (Fig. 4), indicating that the intermediate was well stabilized in the microenvironment of subunit *D*, while the product was moderately stabilized in the other subunit.

The asymmetric binding of the inhibitor and the bidentate binding of the intermediate and the product at the active site in APD strongly imply that 2AP, the substrate of APD, binds the iron in such a mode that its deprotonated hydroxyl occupies the position opposite Glu251 and the amino group binds at the site *trans* to His62. Based on these structural data and on comparison with the ligand-binding schemes observed in published structures, such as 4,5-PCD (Sugimoto *et al.*, 1999), DHBP (Sato *et al.*, 2002) and HPCD (Kovaleva &

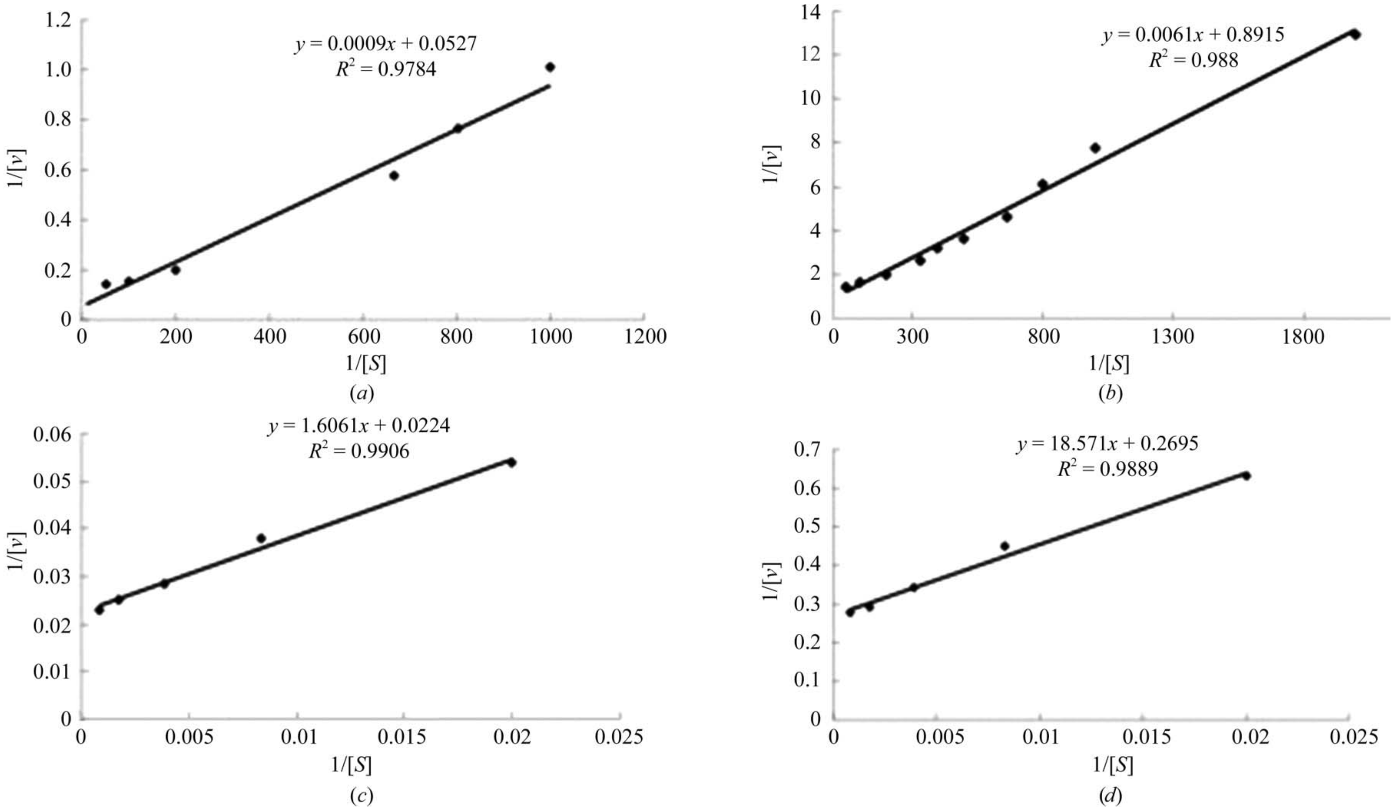

Figure 7
Lineweaver–Burke plots of APD with 2AP (*a*) and catechol (*b*) under aerobic conditions, as well as those with a controlled O_2 concentration from 0 to 1200 μM using 2AP (*c*) and catechol (*d*) as the substrates. Assays were carried out in phosphate buffer at pH 8.0. The concentration of purified APD was 0.015 mg ml^{-1}.

Lipscomb, 2007), we can confidently conclude that APD utilizes a similar catalytic mechanism on its substrate, which can be summarized in Fig. 1. At the beginning of the reaction cycle, 2AP accesses the enzyme active site and binds Fe(II) asymmetrically (Fig. 1*b*). The binding of 2AP to the iron efficiently lowers the barrier to O_2 binding at the adjacent site *trans* to His13 (Fig. 1*c*). Spectroscopic and previous crystallographic studies have suggested that simultaneous binding of the substrate and O_2 allows immediate electron transfer from the former to the latter *via* Fe(II), resulting in concerted activation of both components (Arciero & Lipscomb, 1986; Shu *et al.*, 1995; Kovaleva & Lipscomb, 2007). Spectroscopic data for APD are unfortunately lacking, but it seems reasonable to propose that O_2 binding and electron transfer are also coupled in this case, leading to the formation of a nascent superoxide (Fig. 1*d*). Presumably, in the subsequent steps an alkylperoxo intermediate is formed owing to recombination of the incipient radicals (Fig. 1*e*) before O—O bond cleavage and insertion of one O atom into the aromatic ring to form a lactone intermediate (Fig. 1*f*) and generation of the product with opened ring (Fig. 1*g*), as observed *in cystallo*.

Despite the similar mechanistic strategy shared by APD and canonical dioxygenases, the intriguing question concerning how APD distinguishes its substrate from catecholic compounds, which are structurally alike, remains unclear. Biochemical studies have shown that APD is very sensitive to catecholic compounds. The enzyme becomes completely inactivated in the presence of a very low concentration of catechol or 4NC, but is never autoinhibited by its substrate 2AP (Lendenmann & Spain, 1996; Davis *et al.*, 1999; Wu *et al.*, 2005). The high degree of substrate specificity indicates that the enzyme must have evolved some structural mechanism to sense the subtle difference between its substrate and the inhibitor.

As the most striking feature, the Fe ligation in APD is enantiomeric to that in HPCD, which results in the generation of a noteworthy aligned $O^-—Fe^{2+}—O^-$ species prior to O_2 binding (Fig. 6*a*). A rational scenario is that the decrease in the Fe(II)/Fe(III) redox potential resulting from this species upon catecholic compound binding is probably greater than that upon 2AP binding, as the adjacent –OH group in catechol is replaced by an $–NH_2$ group in 2AP. Owing to the formation of the aligned $O^-—Fe^{2+}—O^-$ species, the iron redox potential may decrease to a more pronounced extent than in other species in which the two monoanions are not aligned, *e.g.* as is the case in HPCD. The sharp change in the Fe redox property upon catecholic compound binding at the active site of APD in turn renders Fe(II) too reductive to lose an electron to O_2 binding at the adjacent position; the ferrous centre is thus oxidized to a ferric centre and the enzyme becomes inactivated. Upon 2AP binding, however, the decrease in Fe redox potential may not be so pronounced as to make Fe(II) lose an electron and be oxidized to Fe(III). This scenario could account for the fact that APD is more sensitive to catecholic compounds than HPCD, but is not autoinhibited by 2AP.

Another possibility is that the high degree of substrate specificity shown by APD might be dependent on the ligand effective concentration (EC). Although structurally alike, some chemical properties of the substrate and the inhibitor are not comparable. The theoretical pK_a values of 2AP and catechol are 10.35 and 9.34, respectively, as calculated by the program *MarvinSketch* (ChemAxon), meaning that 2AP has a tenfold weaker ability to deprotonate in solution than its catecholic counterpart. In other words, it means that the EC of the monoanion of 2AP, *i.e.* the activated substrate, is lower than that of activated inhibitor by one order of magnitude, given equal amounts of these two chemicals in solution. Therefore, even if the decrease in the Fe(II)/Fe(III) redox potential upon catecholic compound binding is comparable to that upon 2AP binding, APD may not be inactivated by 2AP binding on account of the lower EC of the activated substrate, and APD can thus tolerate a much higher concentration of 2AP than of catecholic compounds.

No matter which scenario is the real case, further investigations are needed to clarify the structural determinants of noncatecholic substrate specificity, not only from the perspective of crystallography but also from spectroscopic and computational studies.

This work was supported by the ‘973’ Project (2011CB910304 and 2013CB911500) and the National Natural Science Foundation (30725001, 31270788 and 31270792) in China. The authors are grateful to the beamline staff at NW12A of KEK, Photon Factory, Japan for data collection.

References

Arciero, D. M. & Lipscomb, J. D. (1986). *J. Biol. Chem.* **261**, 2170–2178.

Bruijnincx, P. C., van Koten, G. & Klein Gebbink, R. J. (2008). *Chem. Soc. Rev.* **37**, 2716–2744.

Brünger, A. T., Adams, P. D., Clore, G. M., DeLano, W. L., Gros, P., Grosse-Kunstleve, R. W., Jiang, J.-S., Kuszewski, J., Nilges, M., Pannu, N. S., Read, R. J., Rice, L. M., Simonson, T. & Warren, G. L. (1998). *Acta Cryst.* D**54**, 905–921.

Davis, J. K., He, Z., Somerville, C. C. & Spain, J. C. (1999). *Arch. Microbiol.* **172**, 330–339.

Doublié, S. (1997). *Methods Enzymol.* **276**, 523–530.

Horsman, G. P., Jirasek, A., Vaillancourt, F. H., Barbosa, C. J., Jarzecki, A. A., Xu, C., Mekmouche, Y., Spiro, T. G., Lipscomb, J. D., Blades, M. W., Turner, R. F. & Eltis, L. D. (2005). *J. Am. Chem. Soc.* **127**, 16882–16891.

Iwagami, S. G., Yang, K. & Davies, J. (2000). *Appl. Environ. Microbiol.* **66**, 1499–1508.

Jones, T. A., Zou, J.-Y., Cowan, S. W. & Kjeldgaard, M. (1991). *Acta Cryst.* A**47**, 110–119.

Kleywegt, G. J. (2007). *Acta Cryst.* D**63**, 94–100.

Koehntop, K. D., Emerson, J. P. & Que, L. (2005). *J. Biol. Inorg. Chem.* **10**, 87–93.

Kovaleva, E. G. & Lipscomb, J. D. (2007). *Science*, **316**, 453–457.

Kovaleva, E. G. & Lipscomb, J. D. (2008*a*). *Biochemistry*, **47**, 11168–11170.

Kovaleva, E. G. & Lipscomb, J. D. (2008*b*). *Nature Chem. Biol.* **4**, 186–193.

Laskowski, R. A., MacArthur, M. W., Moss, D. S. & Thornton, J. M. (1993). *J. Appl. Cryst.* **26**, 283–291.

Lendenmann, U. & Spain, J. C. (1996). *J. Bacteriol.* **178**, 6227–6232.

Li, D.-F., Zhang, J.-Y., Hou, Y., Liu, L., Liu, S.-J. & Liu, W. (2012). *Acta Cryst.* F**68**, 1337–1340.

Murshudov, G. N., Skubák, P., Lebedev, A. A., Pannu, N. S., Steiner, R. A., Nicholls, R. A., Winn, M. D., Long, F. & Vagin, A. A. (2011). *Acta Cryst.* D**67**, 355–367.

Noda, Y., Nishikawa, S., Shiozuka, K., Kadokura, H., Nakajima, H., Yoda, K., Katayama, Y., Morohoshi, N., Haraguchi, T. & Yamasaki, M. (1990). *J. Bacteriol.* **172**, 2704–2709.

Rossmann, M. G. & van Beek, C. G. (1999). *Acta Cryst.* D**55**, 1631–1640.

Sato, N., Uragami, Y., Nishizaki, T., Takahashi, Y., Sazaki, G., Sugimoto, K., Nonaka, T., Masai, E., Fukuda, M. & Senda, T. (2002). *J. Mol. Biol.* **321**, 621–636.

Shu, L., Chiou, Y. M., Orville, A. M., Miller, M. A., Lipscomb, J. D. & Que, L. (1995). *Biochemistry*, **34**, 6649–6659.

Straganz, G. D. & Nidetzky, B. (2006). *Chembiochem* **7**, 1536–1548.

Sugimoto, K., Senda, T., Aoshima, H., Masai, E., Fukuda, M. & Mitsui, Y. (1999). *Structure*, **7**, 953–965.

Takenaka, S., Murakami, S., Shinke, R., Hatakeyama, K., Yukawa, H. & Aoki, K. (1997). *J. Biol. Chem.* **272**, 14727–14732.

Terwilliger, T. (2004). *J. Synchrotron Rad.* **11**, 49–52.

Vaillancourt, F. H., Barbosa, C. J., Spiro, T. G., Bolin, J. T., Blades, M. W., Turner, R. F. & Eltis, L. D. (2002). *J. Am. Chem. Soc.* **124**, 2485–2496.

Vaillancourt, F. H., Bolin, J. T. & Eltis, L. D. (2006). *Crit. Rev. Biochem. Mol. Biol.* **41**, 241–267.

Winn, M. D. *et al.* (2011). *Acta Cryst.* D**67**, 235–242.

Wu, J.-F., Jiang, C.-Y., Wang, B.-J., Ma, Y.-F., Liu, Z.-P. & Liu, S.-J. (2006). *Appl. Environ. Microbiol.* **72**, 1759–1765.

Wu, J.-F., Sun, C.-W., Jiang, C.-Y., Liu, Z.-P. & Liu, S.-J. (2005). *Arch. Microbiol.* **183**, 1–8.

Zhang, Z., Ren, J., Stammers, D. K., Baldwin, J. E., Harlos, K. & Schofield, C. J. (2000). *Nature Struct. Biol.* **7**, 127–133.